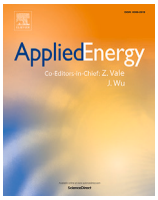
Applied Energy 427 (2027) 128914



Contents lists available at ScienceDirect

Applied Energy

journal homepage: www.elsevier.com/locate/apen



Data-driven modeling and optimization of anode-side structural, transport and electrochemical properties in PEM water electrolyzers

K. Ashoke Raman[a,*], Linus Hammacher[a,b], Violeta Karyofylli[a], Hans Kungl[a], André Karl[a], Eva Jodat[a], Rüdiger-A. Eichel[a,b,c]

[a] Institute of Energy Technologies, Fundamental Electrochemistry (IET-1), Forschungszentrum, Jülich, 52425, Germany
[b] Institute of Physical Chemistry, RWTH Aachen University, Aachen, 52062, Germany
[c] Faculty of Mechanical Engineering, RWTH Aachen University, Aachen, 52062, Germany

HIGHLIGHTS

- Development of two ANN models to predict cell performance and voltage losses.
- SHAP based feature screening to select most influential features and perform data reduction.
- Ionomer content and exchange current density are key properties influencing cell performance.
- A genetic algorithm is combined with an ANN surrogate model to perform parameter optimization.

ARTICLE INFO

Keywords:
Machine learning
Feature selection
PEM water electrolyzer
Voltage losses

ABSTRACT

Proton exchange membrane water electrolyzers are intricate multiphysics systems, whose commercial scale up and viability depend on optimizing the structural/material design of their cell components. Some of these structural properties also influence reactivity of the catalyst layers. The sluggish kinetics on anode side is of particular interest as the main water splitting reaction occurs on this part of the electrolyzer. Unlike PEM fuel cells, the public availability of experimental datasets is still limited. Therefore, in this work we undertake a data-driven approach using synthetic data generated from physics-based numerical model to investigate the effects of important structural, transport and electrochemical properties on cell performance. To facilitate model training through dimensionality reduction, Shapley additive explanations based feature selection procedure is adapted. Two separate artificial neural network models were trained on the reduced dataset to predict cell performance and voltage losses. Parametric analysis shows that based on the selected input properties, the ionomer volume fraction and absolute permeability of the porous transport layer are the important structural properties which influence cell performance. Voltage loss decomposition analysis corroborates these observations. Finally, the surrogate model was employed as the objective function within the genetic algorithm to determine the optimal input feature values. The optimized structural, transport and electrochemical properties demonstrated an improved cell performance when compared to the selected baseline values.

1. Introduction

Efficient transport of chemical species to and from the reaction zone constitutes one of the fundamental aspects governing the optimal performance of a proton exchange membrane water electrolyzer. To sustain high reaction rates and minimize overpotentials, it is pertinent that the associated transport processes, such as the delivery of liquid water to the catalyst layer, removal of generated gases, and electronic/protonic transfer are executed efficiently [1]. The structural, electrochemical and transport properties of the catalyst and proton transport layers thus emerge as critical factors in governing these transport phenomena. Catalyst layer porosity and tortuosity determine the accessibility of Iridium particles to hydrated ionomer and water. As such, they constitute some of the important factors which govern the actual electrochemical active surface area (ECSA). Efficient removal of oxygen gas bubbles is governed by pore connectivity and permeability of both

* Corresponding author.
Email address: r.kuppa@fz-juelich.de (K. Ashoke Raman).

https://doi.org/10.1016/j.apenergy.2026.128914
Received 13 April 2026; Received in revised form 4 July 2026; Accepted 16 September 2026

0306-2619/© 2026 The Authors. Published by Elsevier Ltd. This is an open access article under the CC BY license (http://creativecommons.org/licenses/by/4.0/).
Open access funding enabled and organized by Projekt DEAL.

Nomenclature

Abbreviations

ANN	Artificial Neural Network
CFD	Computational Fluid Dynamics
CL	Catalyst Layer
ESCA	Electrochemical Active Surface Area
HER	Hydrogen Evolution Reaction
KNN	K Nearest Neighbors
MAE	Mean Absolute Error
MEA	Membrane Electrode Assembly
ML	Machine Learning
MSE	Mean Square Error
OER	Oxygen Evolution Reaction
PEM	Proton Exchange Membrane
PEMFC	Proton Exchange Membrane Fuel Cell
PEMWE	Proton Exchange Membrane Water Electrolyzer
PTL	Porous Transport Layer
RMSE	Root Mean Square Error
SHAP	Shapley Additive Explanations
SVM	Support Vector Machines
SVR	Support Vector Regression
XGB	Extreme Gradient Boosting

Symbols

ϵ_{acl}^{ion}	Ionomer volume fraction in anode CL
ϵ_{cl}^{a}	Porosity of anode CL
ϵ_{ptl}^{a}	Porosity of anode PTL
η_a	Anodic overpotential
η_c	Cathodic overpotential
κ_{cl}^{a}	Absolute permeability of anode CL
κ_{ptl}^{a}	Absolute permeability of anode PTL
σ_{cl}^{a}	Electrical conductivity of anode CL
τ_{cl}^{a}	Tortuosity of anode CL
τ_{ptl}^{a}	Tortuosity of anode PTL
$\triangle\phi_e$	Electron transport voltage loss
$\triangle\phi_p$	Proton transport voltage loss
$j_{o,a}^{ref}$	Reference exchange current density
K_{cl}^{a}	Thermal conductivity of anode CL
K_{mem}	Thermal conductivity of membrane
n_s	Coverage exponent of anode catalyst layer
R^2	Coefficient of determination

the PTL and CL. These structural properties [2,3] control the capillary pressure gradients and gas-phase percolation pathways. Adequate ionomer content in the CL is pivotal for facilitating ionic transport; however, excessive ionomer content also hinders electronic conductivity in the catalyst layer which is typically detrimental to cell performance. Transport properties such as thermal and electronic conductivity determine the ohmic losses and heat removal efficiency arising due to the movement of electrons and protons. Therefore, it is essential to not only understand the effect of these structural and transport properties on the cell performance, but also to actively tune them to achieve enhanced operational efficiency.

Local reaction rates and overpotentials are governed by the coupled transport of protons, electrons, liquid water and gas bubbles. Structural properties such as porosity, permeability and tortuosity of the catalyst and porous transport layers dictate these processes [4–6]. Five different PTLs with varying porosity and pore diameter were used to evaluate the performance of a PEMWE [7]. Small pore sizes were found to be beneficial for water transport and large pores for gas removal. They found that in addition to porosity, the in-plane and through-plane permeabilities were key parameters for characterizing how PTL structures affect PEM water electrolysis. An increase in catalyst layer porosity favored reduction in activation overpotentials; however, higher ohmic losses were noted due to decrease in ionomer mass fraction [8]. Losses due to mass transfer were quantified using electrochemical impedance spectroscopy for different PTL structural properties [9]. An optimum porosity of 0.6 was obtained experimentally that showed optimal mass transfer performance. In terms of tortuosity, mass transfer losses were reduced with lower tortuosity. Three-dimensional reconstruction via Focused ion beam- scanning electron microscopy (FIB-SEM) images revealed that heterogeneous porosity and tortuosity are exhibited throughout the thickness of the catalyst layer which affect local transport paths of water and gaseous oxygen [10]. The effect of varying anode porosity was investigated through a three dimensional two-phase numerical model of a PEMWE. An optimal porosity window between 50–60% was identified and the use of a PTL with graded porosity was proposed [11].

Structural properties determine the pathways and pore network for fluid flow and ionic/electronic transport. Voltage losses arising from these properties are attributed to the blockages encountered along these pathways restricting reactant flow, obstructing product removal and extending electronic/ionic pathways [11]. The effective transport properties, on the other hand, are intrinsic bulk characteristics of material which are also dependent on its distribution and contact interfaces. Electronic conductivity of the catalyst layer governs the in-plane and through-plane resistance, thereby, facilitating the ease with which these electrons propagate from the reaction sites to the PTL [12–14]. Increasing electronic conductivity increases cell performance due to reduction in contact resistance between the catalyst and porous transport layer and enhanced availability of catalyst particles participating in the electrochemical reaction [15,16]. The passage of electrons through the catalyst layer/bipolar plates and protons across the membrane generate substantial ohmic heating. This results in the formation of local hot spots and thermal gradients across the catalyst layers which hinder cell performance and accelerate membrane degradation [17]. Therefore, the thermal conductivity of the catalyst layer and membrane plays a crucial role in mitigating these problems through efficient heat dissipation [18,19]. Better thermal management ensures that the temperature is uniformly distributed and reduces voltage losses.

The literature reviewed above highlights the necessity of optimizing the structural and effective transport properties of individual cell components to enable scaling and commercial viability. Tuning these parameters will prevent mass transport losses and maintain stable operation by preventing voltage spikes resulting from gas accumulation. Tailoring structural and effective transport properties would drive efficient catalyst activation and thermal stability. Optimizing both these types of categorical properties would ensure lower cell voltages and extended lifetimes of PEM water electrolyzers [20]. The most straightforward approach is to conduct a systematic experimental investigation to screen for the optimum parametric values. However, given the number of parameters and their corresponding value ranges, this approach is ineffective in terms of both time and cost. Operation of PEMWE spans across varying length and time scales which is governed by the complex interplay of electrochemistry, flow and heat transport [21,22]. As such, insights into these internal physics reflecting on how different parameters influence cell performance are limited when performing only experimental trials. Physics based numerical models circumvent these drawbacks. Numerical modeling provides a cost effective framework for systematically screening through the parameter space [23,24]. Simulations allow detailed physical insights by enabling probing into how variations in different structural and material properties influence cell performance and losses [25,26]. The bottleneck in using high fidelity

3D models to investigate structural properties lies in their computational demand. Creating models which accurately resolve across all varying length scales, from pore scale microstructures to macroscale cell components, requires a larger computation domain with fine spatial discretization. This incurs significant memory and computational run times. Machine learning based data-driven modeling has emerged as a viable approach with the ability to overcome these limitations [27,28]. Machine learning algorithms learn patterns from experimental or numerical data, and establish relationships between input parameters and output variables. Once trained, these models offer real-time inference and prediction capabilities.

Machine learning methods have been predominantly applied to screen electrocatalysts in the field of PEMWEs [29–31]. Efforts in employing these techniques to analyze the effect of different parameters on cell performance at a macroscopic level are still in their early stages when compared with similar studies on PEMFCs [28,32]. A database generated from existing literature has been used to identify critical parameters influencing cell performance [33]. Pore structure, ionomer content and catalyst loading were identified as important parameters. The database is extracted from 789 experimental findings in 30 publications. A combination of SHAP, KNN and Bayesian optimization methods was used for this analysis. More recently, a database with over 1000 experimental samples from 127 publications was used to develop data-driven models [34]. The database comprised 85 parameters related to material selection, MEA fabrication, cell assembly and characterization. The XGB model was deployed to quantify feature importance. Machine learning has been adapted to optimize experimental cell design for PEMWEs. A combination of decision trees and KNN models was used to design flow field patterns which improve hydrogen production efficiency [35]. The model was trained and validated with 1062 design data points which included electrode area, type of cell design, anode and cathode flow areas. Similar design endeavors were undertaken to optimize hydrogen production rate using polynomial and logistic regression models [36]. Model comparison with a custom made cell using the parameters predicted by the data-driven models showed good agreement with experimental measurements. Experimental data based machine learning modeling has been pursued to investigate the impact of operational parameters such as temperature, torque and flowrate on cell performance [37]. Evaluation based on MAE showed that the support vector machine performs better than random forest and multi-layer perceptron algorithms in predicting current density and hydrogen flowrate. Using experimental cell data in the form of polarization curves and impedance measurements, the effect of three different pre-conditioning procedures was evaluated using the extreme gradient boosting algorithm [38]. The subsequent SHAP analysis revealed that for short run operations thermal conditioning showed best relative performance improvement. When compared with PEMFCs, only few works in literature have showcased the combination of experiments and data-driven modeling in the context of PEMWE [39] owing to the scarcity of public datasets. In this context, synthetic data generated from numerical models emerges as a viable option to pursue the integration of data-driven modeling with PEMWEs.

The data generated from numerical models are obtained by solving equations grounded in physical laws. Moreover, these synthetic datasets are clean and do not contain noise typical of experimental data. This enables data-driven models to identify and learn the underlying patterns more readily. The effect of important operating parameters and transport properties on the performance of PEMWE was investigated for supported and unsupported catalysts [16]. A one-dimensional PEMWE numerical model was used to generate the synthetic dataset. SHAP analysis revealed that in case of supported catalyst layers, the membrane thickness has a higher influence than electronic conductivity on the output current density. Owing to the real time inference of data-driven models, they are efficient at performing uncertainty quantification [40] and have been used to list important parameters influencing parasitic currents in PEMWE. A CFD-data driven approach was undertaken to investigate the effect of cell temperature, PTL thickness, membrane thickness and applied voltage on cell performance [41]. Four different models were used and SVR was selected as the best performing method. Based on the above literature on PEMWE, we notice that studies have primarily focused on deploying machine learning to investigate the effect of operating and design parameters on the cell performance. Even though the structural and material properties play a critical role in governing the performance of PEMWE, efforts in data-driven modeling along this direction remain unexplored. The present work attempts to fill this gap in knowledge. In order to do so, we have selected 12 different structural and material properties to generate a synthetic dataset using a one-dimensional numerical model [23]. Full factorial design approach is used to generate the synthetic data. To optimize model training, we have used SHAP-based ranking to perform feature selection. This approach enables an interpretable approach to identifying most influential features that affect the output current density and reduces the dimensionality without compromising prediction accuracy. The physics-based model which is used to generate the synthetic data is operated galvanostatically. Thereby, following the findings of our previous investigation [16], we have selected ANN to proceed with parametric analysis as it has shown good performance even for extrapolation. To decompose the overall behaviour, we have used two different ANN models to predict cell performance and voltage losses. Finally, to illustrate the advantage of deploying data-driven models in providing real-time inference, we have used the trained model for optimization. Based on the selected parameter space, optimization using a genetic algorithm is performed to screen for the best parameter combination that predicts maximum current density.

The paper is organized as follows: Section 2 describes the details of data curation procedure. This section also briefly outlines the XGB and ANN methods. Section 3 describes the results with discussion of SHAP-assisted feature selection, parametric analysis and optimization. Concluding remarks are provided in Section 4.

2. Methodology

The synthetic dataset is generated using the 1D two-phase non-isothermal numerical model for a PEMWE [23]. The model solves a coupled non-linear system of nine governing equations which account for mass, species, heat and charge transport. The model has already been validated against experimental measurements [42,43] and shows good agreement. Therefore, the synthetic data generated from this numerical model serve as a validated computational database for developing an accurate and clean data-driven model. A full factorial design sampling is used to generate the data in which all possible combinations of levels of all input factors are systematically computed. Table 1 illustrates the list of all parameters.The parameters were categorized into structural or morphological and material properties. A total of 8 structural and

Table 1
Parameter groups for anode side of PEM water electrolyzer. The underlined values refer to the baseline values which are used in parametric analysis.

Structural properties	Unit	Values	Reference
Coverage exponent of aCL	—	[2, 4, 6]	[23]
Absolute permeability of aPTL	m^2	[1, 10, 100]×10^{-13}	[3]
Absolute permeability of aCL	m^2	[1, 50, 75]×10^{-15}	[10,23]
Porosity of aPTL	—	[0.3, 0.45, 0.6, 0.8]	[6,23]
Porosity of aCL	—	[0.15, 0.35, 0.55]	[10,40]
Tortuosity of aPTL	—	[1.1, 1.8, 2.5]	[3]
Tortuosity of aCL	—	[1.1, 2.5, 5]	[10]
Ionomer volume fraction in aCL	—	[0.1, 0.2, 0.3, 0.4, 0.5]	[10,40]
Transport/electrochemical properties			
Electrical conductivity of aCL	S/m	[3.5, 35, 350]	[23]
Thermal conductivity of aCL	W/(m·K)	[0.27, 0.87, 3]	[23,44]
Thermal conductivity of PEM	W/(m·K)	[0.11, 0.33, 0.66]	[45]
Reference exchange current density	A/m^2	[1,4,8,13.2]×10^{-3}	[21]

4 transport/electrochemical properties were considered. The values or levels of each parameter used in generating the data are also provided in the table. The data was generated with the MATLAB code which was run on the supercomputing cluster. The generated dataset comprised a total of 21,140,071 data points. Further data processing was accomplished using Jupyter Notebook. As input features vary across different scales, it is customary in machine learning to scale these features before model training. We have scaled all the features between 0 and 1. While a 1D physics-based model is efficient in generating a large database required to train accurate machine learning models, it is important to acknowledge its limitations. Dominant diffusive transport phenomena occur along the through-plane direction. A robust 1D model captures these through plane effects accurately [8,21,23,46]. However, there are in-plane effects which result from non-uniformity in concentration and temperature gradients along the planar direction. The in-plane conductivity, for example, is influenced by these factors [12]. The complex two phase dynamics of gas bubbles within the porous layers and flow field channels lead to mass transfer losses. In order to account for such localized spatial phenomena, it is necessary to train on data obtained from higher 3D numerical models or experiments [3,10,25,41,47].

Two different machine learning algorithms were used in this study. Firstly, extreme gradient boosting (XGB) was applied to the generated dataset to predict the output current density. After hyperparameter tuning and model training, we conducted SHAP analysis using the trained XGB model to quantify feature importance based on their contribution to the model's predictions. Based on SHAP ranking, most influential features were identified, leading to a reduction of the original high-dimensional dataset to a subset consisting of dominant input features. Subsequently, two separate ANN models were developed to predict cell performance and voltage losses. We discussed the details of XGB and ANN in our previous work [16,40], to which interested readers may refer for further information.

3. Results and discussion

We commence our discussion on results by first investigating the importance of feature selection using SHAP methodology. This will be followed by evaluating the model performance and validating it on unseen test data. We then study the impact of the selected structural and material properties, obtained from feature selection, on the cell performance. Finally, using genetic algorithm we obtain the optimum values of these parameters which improve cell performance.

3.1. Feature selection: SHAP analysis

Previously, we have observed that the ANN shows better model performance than XGB model, especially when testing with parameter values residing outside the training domain [16]. This is attributed to the ANN model's architecture comprising multiple hidden layers and non-linear activation nodes, which enable accurately establishing the input–output relationship between features and performance indicators. However, it is well known that if ANNs are trained on high-dimensional data, they can lead to spurious correlations if irrelevant or redundant features are not removed. As noted from Table 1, the dataset for voltage prediction comprises 12 input features and would lead to higher computational cost. This increase in computational cost for training can be reduced with the removal of weak features. To accomplish this task, we use SHAP-based feature selection to rank the input parameters based to their marginal contribution on model prediction. The XGB model is first trained on the dataset and SHAP values are computed for all the features. Owing to the additive tree-based nature of the XGB algorithm, the SHAP explainer uses the internal trees to compute the per-feature contribution by tracing the decision paths. The efficiency in computing SHAP values with XGB model lies in utilizing the high-speed TreeSHAP algorithm, which calculates the average difference for all possible feature combinations in polynomial time, instead of the usual exponential time. Subsequently, the features with low SHAP values can be safely removed without compromising model prediction.

Before we proceed to perform feature selection, it is pertinent to identify if one or more input parameters are highly correlated. Coupled features impose the problem of identifying which feature drives the model outcome and increase the ambiguity in assigning appropriate importance to a parameter that is actually unique. On the other hand, early detection of correlated parameters could help in dropping one of them, thereby reducing the dimensionality of the model. Fig. 1(a) shows the correlation matrix where the majority of the off diagonal cells have values close to 0.0. This implies that there is a high degree of independence between the input parameters and changing one parameter will not affect the other. This information is particularly important when performing optimization, as individual parameters could be tuned independently. We only notice a weak positive correlation of 0.14 between n_s and κ^a_{cl}. While we observe weak correlations between the input features in Fig. 1(a), it is to be noted that parameters such as porosity, tortuosity and electronic conductivity exhibit a high degree of physical coupling. The low correlation shown in our dataset arises due to the synthetic data generation process. The full factorial sampling strategy, varied across the selected parametric combinations enforces statistical independence.

The data for performing SHAP analysis consist of the 12 input features, as listed in Table 1, and the current density as the output variable. This leads to a dataset comprising 21,140,071 data points. A test size of 0.2 is used to split the data into train and test datasets and the XGB model is employed to train the regression model. After screening different hyperparameter values, the total number of estimators is set to 900. The model parameters *max depth* and *learning rate* were set to 9 and 0.025, respectively. Model training was performed on a GPU cluster, which took an approximate training time of 70 s. In the context of model performance, the RMSE values of 0.002 and 0.0021 were obtained on the training and test data, respectively. From the summary plot illustrated in Fig. 1(b), we observe that the ionomer volume fraction (ϵ^{ion}_{acl}) is the predominant factor influencing the current density with a mean SHAP value of 0.0226. It shows positive correlation with current density. With a mean SHAP value of 0.0215, κ^a_{PTL} is the second most influential parameter affecting the model's prediction of current density. Since PTL permeability controls the pressure drop in the two-phase flow, it exhibits a positive correlation with current density. Both ϵ^{ion}_{acl} and κ^a_{ptl} are characterized by a high mean and high spread distribution (SHAP value ranging from -0.15 to 0.075) on the SHAP summary plot. This is unlike the next two parameters, wherein $j^{ref}_{o,a}$ has a higher mean SHAP value (0.0189) than κ^a_{CL} (0.0171), but shows a lower spread. This implies that $j^{ref}_{o,a}$ has a consistent contribution to the model's output, independent of the specific combination of feature values. The larger spread in SHAP values for κ^a_{CL}, particularly in the negative direction up to -0.15, indicates that its contribution to the model's output in scenarios where κ^a_{cl} is low has a higher impact than that of $j^{ref}_{o,a}$. The coverage exponent (n_s) and electronic conductivity (σ^a_{cl}) rank next with a mean SHAP value of 0.0107 and 0.0052, respectively. The negative SHAP correlation of n_s implies that larger coverage exponents usually predict lower current density at the same cell potential. Although τ^a_{cl} has a low mean SHAP value of 0.00054, its spread is comparable with that of σ^a_{cl}. As such, we have considered this feature for further model development. The other parameters have a mean SHAP value of less than 0.0002. This implies that the changes in the values of these features affect the model's output by less than 0.02%. Therefore, we have considered them as weak features and removed corresponding entries from the original database. After performing feature selection using SHAP, we have selected a total of seven input parameters including five structural and two material properties. While recent data-driven modeling works [16,27,39] for PEMWE have used SHAP as an explainable AI technique to outline important parameters affecting system performance, we have used it as an approach to perform dimensionality reduction.

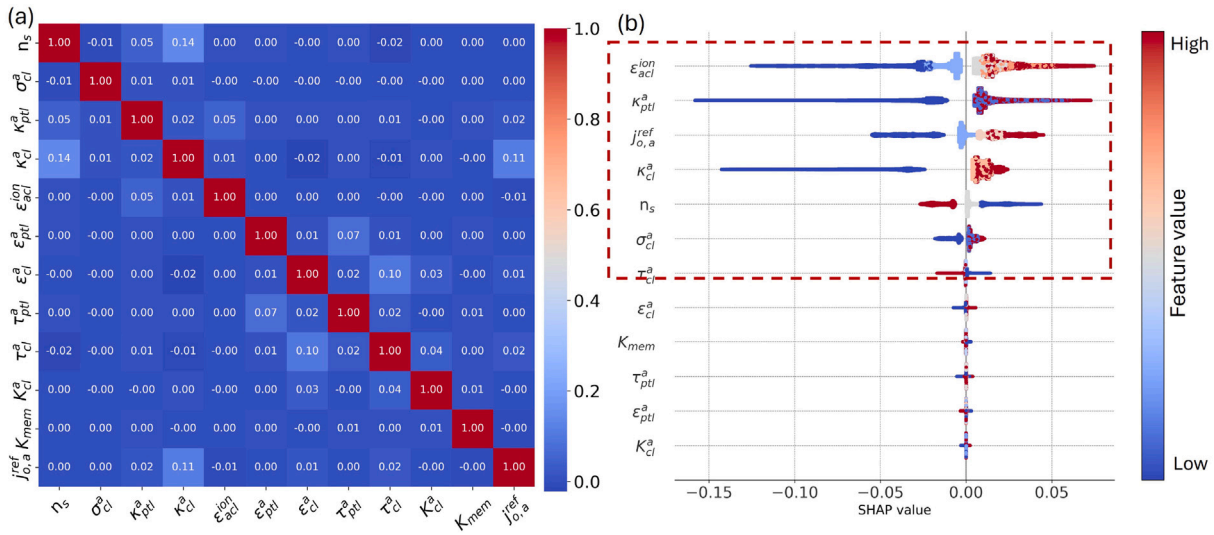


Fig. 1. (a) The correlation matrix showcasing the interactions between different features. (b) The SHAP summary plot showing the important structural and physicochemical properties influencing the current density. The red box lists the features selected on the basis of their SHAP values to train the ANN model.

After removing weak features, the dataset was streamlined to 65,026 data points across seven features. Because the original dataset was structured as a full-factorial grid, fixing these weak features to a single baseline level collapses their varying dimensions. This mathematically reduces the total number of unique parameter combinations from roughly 21 million to 65,026 data points, representing a single, highly refined parametric slice of the original multidimensional space. This reduction highlights the value of SHAP-enabled feature selection in facilitating the computationally efficient training of ANNs. Moving forward, we utilize this optimized dataset to develop two distinct ANN models for predicting output current density and voltage losses.

3.2. Model performance

Before proceeding further, we highlight the necessity of using two separate ANNs for modeling cell performance (j and η_{cell}) and voltage losses: η_a, η_c, $\triangle\phi_p$ and η_c, $\triangle\phi_e$. Cell performance indicators represent system metrics that throw light on the macroscopic output of the electrolyzer. Electrochemical losses, on the other hand, which are reflected in voltage drop and overpotential, are indicative of the underlying mechanistic internal states. Therefore, they facilitate identifying why the cell fails or behaves in a certain way. Moreover, training a single ANN with multiple outputs that have values of varying magnitude creates the problem of *gradient imbalance*. This issue arises when the network assigns higher weights to the gradients associated with current density, computed from the loss function, than those corresponding to voltage losses. Such an imbalance causes the model to prioritize weight updates that minimize current density losses while neglecting voltage losses. In order to consider these two factors, we proceed by utilizing two separate ANNs to model cell performance and voltage losses. The schematic representation of these two different ANN models is illustrated in Fig. 2.

After trying different network architectures, we finalized the decision to build a network with three hidden layers. The number of hidden units in the three layers is set to 60, 40, and 20, respectively. Both the neural network models are built using the same architecture, with ANN-I consisting of two output units and ANN-II having four output units corresponding to the different voltage losses as illustrated in Fig. 2. A total of eight input features, including the input cell voltage, was provided for both the networks. After tuning, the number of epochs and the learning rate for ANN-I were set to be 8000 and 0.001, respectively. ANN-II is designed with the number of epochs set to 2000 and a learning rate of 0.005. The rectified linear unit (ReLU) is used as the activation function for the hidden units. The network directly returns the output values in the raw form through the output layer. The mean square error (MSE) function is selected to compute losses. The models were set up using PyTorch and trained on a GPU cluster provided by the Jülich Supercomputing Center (JSC).

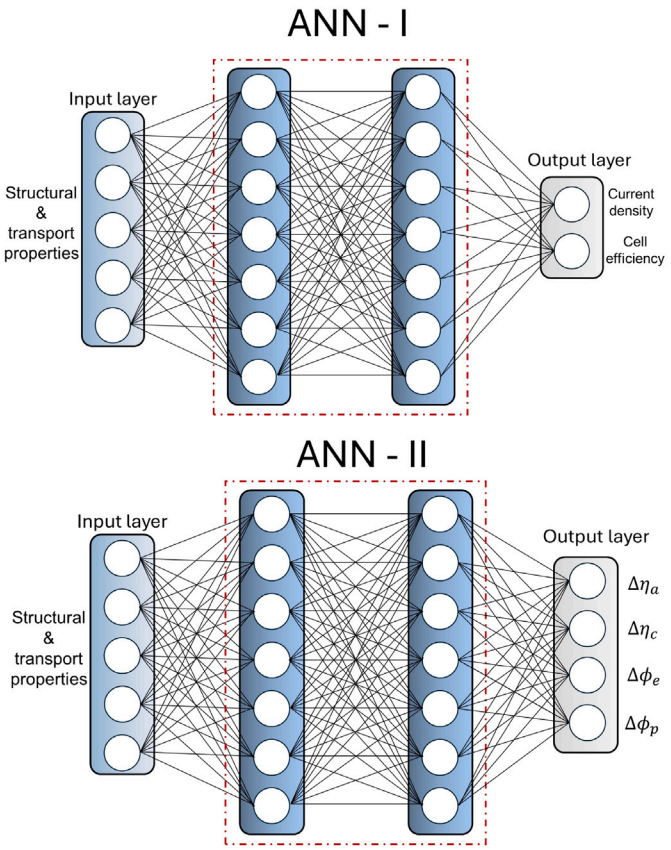


Fig. 2. Schematic representation of ANN-I and ANN-II neural network models which were used to predict cell performance and voltage losses, respectively.

The top row of Fig. 3 illustrates the performance of ANN-I on the training and test datasets. Since the diagonal line represents the case where the predictions are equal to the actual values, the closer the data

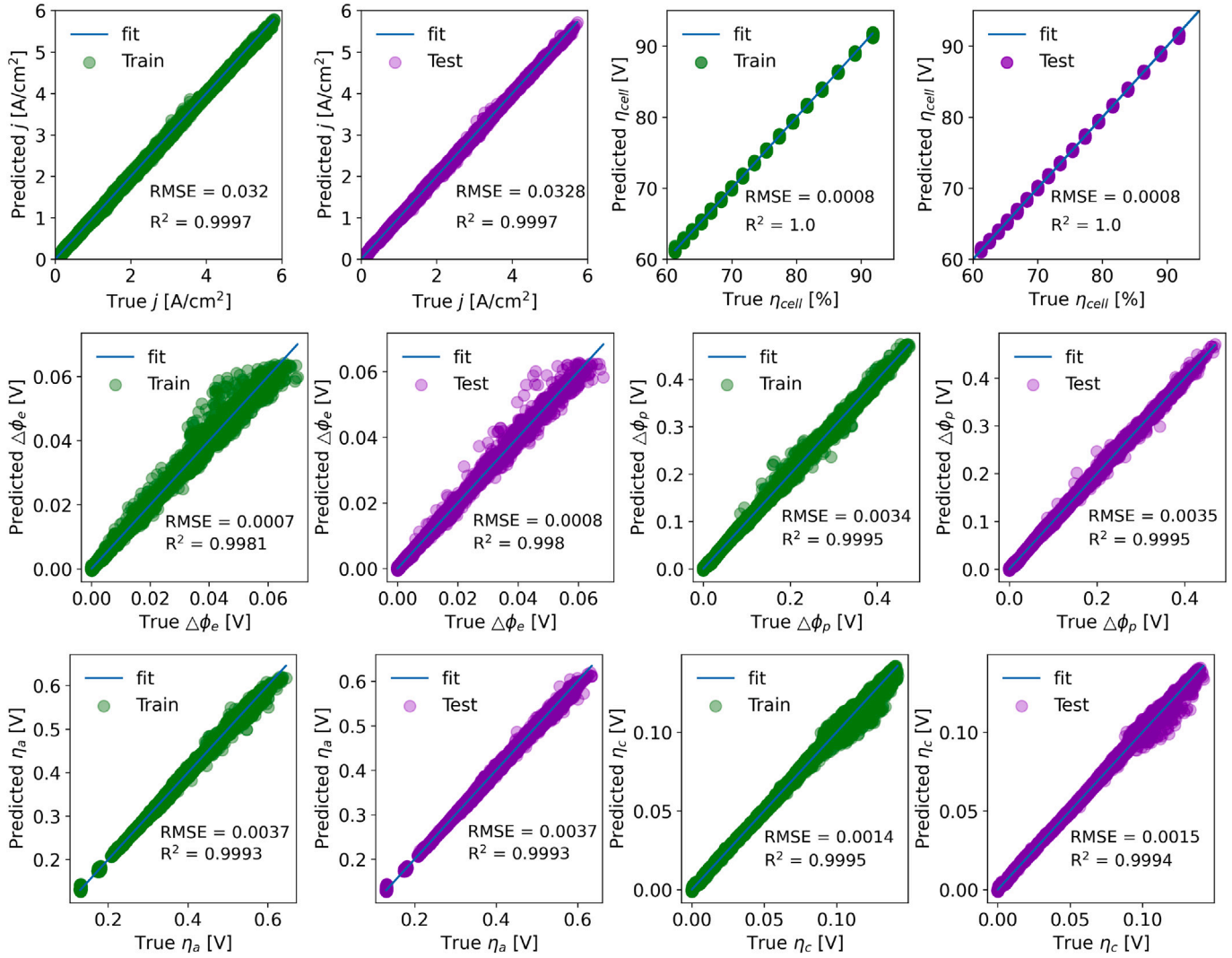


Fig. 3. Model performance illustrated by the fit between the actual and predicted values on the x-axis and y-axis, respectively. Performance on the training (green) and test (violet) data is shown separately, with RMSE and R^2 metrics provided in each figure. Model evaluation for ANN-I, corresponding to current density (j) and cell efficiency (η_{cell}), is shown in the top row. Middle and bottom rows show the model performance of ANN-II for different voltage losses: η_a, η_c, $\triangle\phi_p$ and η_c, $\triangle\phi_e$.

points are located around this line, the better is the accuracy of the ANN model. A tight fit along the diagonal identity line indicates that the model predictions show low variance from the actual values of current density. This low variance is noted from the high R^2 values greater than 0.99 for both training and test datasets. Similarly, with the RMSE values of 0.032 and 0.0328 on the training and test data, the model showcases its accuracy in predicting the output current density. A consistent spread of the data points along the identity line is noted for the entire range of applied cell voltage. Accurate performance of the ANN-I model is also observed for η_{cell} predictions. With an RMSE of 0.0008 and an ideal $R^2 = 1.0$, the model exhibits slightly higher accuracy in predicting η_{cell} when compared to current density. When we compare the performance of ANN-I model based on its RMSE and R^2 values, we observe that for both the training and test datasets it predicts nearly same values. This implies that the model has good generalization and does not show signs of overfitting. Therefore, the model architecture and hyperparameters are well tuned to use this model for further parametric analysis and optimization. The network structure of ANN-I with large number of units in the hidden layer leads to reduced RMSE for predicting current density. It shows better performance when compared to similar data-driven modeling approach [37] using an MLP for PEMWE with experimental data which had the lowest RMSE of 0.0801 for a network structure of 4-6-2-1-1. Similarly, the number of hidden layers for developing an accurate ANN model for PEMWE was found to be four [48]. Beyond a network size of four, the error was seen to increase. In the current work, we have used three hidden layers.

The middle and bottom rows illustrate the performance of ANN-II model which predicts voltage losses. The model displays its accurate performance in predicting $\triangle\phi_e$ with RMSE values of 7×10^{-4} and 8×10^{-4} on the training and test datasets, respectively. The distribution of data points is closer to the identity line for lower cell voltages. However, as the cell voltage increases, we notice the spread of points becomes wider for both training and test datasets. This distribution is characterized by few outliers overpredicting the true $\triangle\phi_e$ at higher cell voltages. While the distribution of data points for $\triangle\phi_p$ is comparatively tighter around the diagonal line, it has a higher RMSE of 3.5×10^{-3} on the test data. A few outliers are observed around the central region corresponding to intermediate applied cell voltages. In terms of model performance for predicting the anodic and cathodic overpotentials, the model performs slightly better in predicting the cathodic overpotential, η_c, with an RMSE of 1.4×10^{-3}, compared to an RMSE of 3.7×10^{-3} for the anodic overpotential, η_a, on the test data. With regard to the distribution of data points,

we see a similar trend of wider spread in the data at higher cell voltages. At higher current densities, the system experiences high mass transport resistances within the catalyst and transport layers. These mass transport losses are induced by steep capillary pressure gradients and non-linear two phase flow dynamics. Therefore, slight variations in structural properties can result in steep variations in overpotentials. This is exhibited by the response of the ANN surrogate model at high current densities

The ANN-II model reports an overall R^2 score greater than 0.99 for all the voltage losses, thereby, exhibiting low variance in model predictions from true values. A notable similarity between ANN-I and ANN-II is that both models demonstrate comparable performance metric values for each output variable on their respective training and test datasets. This shows that the models are less prone to overfitting and can perform well in unseen parameter space.

3.3. Model validation

After investigating the model performance, we now explore further to check the generalization capability of the model on unseen data. This is essential for assessing the model's ability to generalize to new parameter combinations within the design space on which it was trained. The following set of design parameters was used for this purpose: $n_s = 4$, $\kappa^a_{ptl} = 1 \times 10^{-11}$ m^2, $\kappa^a_{cl} = 7.5 \times 10^{-14}$ m^2, $\epsilon^a_{ptl} = 0.8$, $\epsilon^a_{cl} = 0.35$, $\tau^a_{ptl} = 2.5$, $\tau^a_{cl} = 2.5$, $\epsilon^{mem}_{cl} = 0.3$, $\sigma^a_{cl} = 35.0$ S/m, $K^a_{cl} = 0.27$ W/(m.K), $K_{mem} = 0.33$ W/(m.K) and $j^{ref}_{o,a} = 40{,}000$ A/m^2. Fig. 4 illustrates the comparison between numerical results and surrogate model predictions by (a) ANN-I for cell performance and (b) ANN-II for voltage losses. Overall we observe a good overlap between physics-based and data-based model predictions, which emphasizes the fact that ANN-based surrogate modeling is capable of capturing the underlying non-linear relationships governing cell performance and voltage losses for the operated range of cell voltage and design parameters. In particular, we observe from Fig. 4(a) that the ANN-I model not only captures the linear ohmic region accurately, but also the initial steep curve which is controlled by the activation zone. The inverse relationship between the applied cell voltage and η_{cell}, resulting from an increase in internal losses as the applied cell voltage increases, is also well captured by the model.

The predictions made by the ANN-II model to compute the voltage losses are in good agreement with numerical data, as shown in Fig. 4(b). Firstly, the model accurately captures the sharp initial jump of $\triangle\eta_a$ at near zero current density. Numerically, it is a difficult region to capture as the gradient changes rapidly owing to the sluggish OER. Therefore, a good comparison between the physics-based numerical results and the ANN-II model predictions indicates that the latter has included the Butler-Volmer kinetics in its learning patterns from the training data. This is further elucidated as it accurately captures a similar, but less sharp jump in the evolution of $\triangle\eta_c$ with current density on the cathodic side. The transition from activation-based logarithmic to kinetic-governed linear zone with an increase in current density is also captured by the model. The ohmic losses ($\triangle\phi_p$ and $\triangle\phi_e$) are governed by the linear scaling of resistance with current density. The ANN-II model encodes this physical law as it maintains a straight line, even at higher current densities. The model is sensitive enough to resolve even the low $\triangle\phi_e$ which reiterates its capacity to learn physics-based principles from the synthetic training data generated from physics-based numerical model.

After evaluating the model performance, accuracy, and generalization capability, we proceed to a parametric analysis. The effects of key structural and physicochemical properties on cell performance and voltage losses are examined. With the aid of a reliable surrogate model, such a parametric study can be carried out efficiently, thereby circumventing the need for computationally expensive numerical simulations.

3.4. Parametric analysis

As discussed in Section 3.1, we have screened seven input parameters which influence the PEMWE performance. These include five structural and two material properties. In this section, we investigate the effect of each of these parameters on the cell performance and voltage losses using ANN-I and ANN-II, respectively. We first discuss the influence of structural properties in Section 3.4.1, followed by the effects of transport properties in Section 3.4.2. The parametric analysis was performed with values selected both within (interpolation) and outside (extrapolation) the training parameter boundaries.

3.4.1. Effect of structural properties

The top row in Fig. 5 illustrates the influence of n_s and τ^a_{cl} on the current density. The coverage exponent relates to the availability of catalyst surface area, which is usually covered by gas bubbles or intermediate species. We observe that at lower current densities, the variation in n_s does not affect the cell voltage. As the current density increases, we notice the gap between the lines, indicating that the cell performance decreases with an increase in n_s. This is attributed to the fact that an increase in n_s leads to decrease in effective active catalyst surface area. Higher production of oxygen at higher current densities leads to more surface blockage. Therefore, a higher overpotential is required to maintain a given current density. On the other hand, we observe overlapping polarization curves when τ^a_{cl} is varied from 1.8 to 5.8. Tortuosity of the anode catalyst layer measures how twisted the pathways for the reactants and products are, thereby impacting their transport to and from

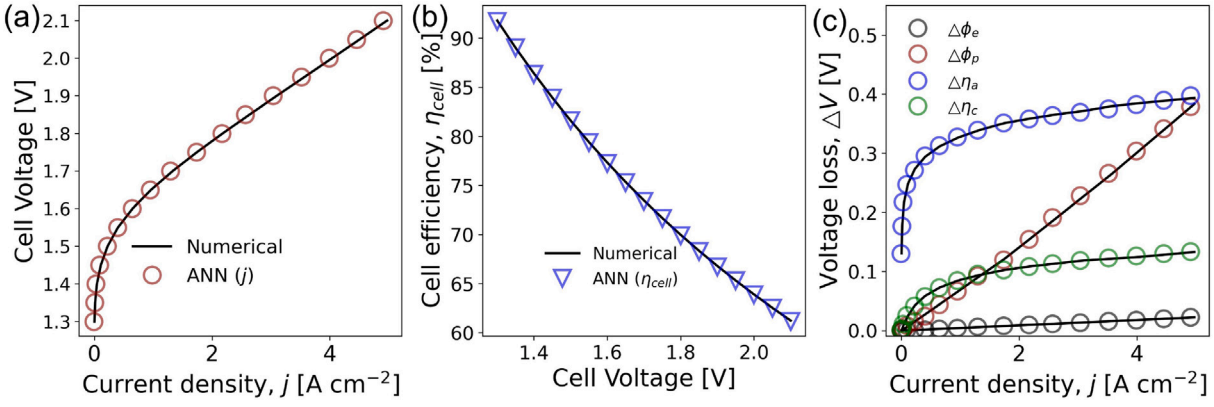


Fig. 4. Validation of the artificial neural network (ANN) surrogate models against the numerical reference model for a previously unseen parameter set. (a) predicted polarization curve (cell voltage vs. current density, j) and (b) cell efficiency (η_{cell}) compared with numerical results. (c) decomposition of voltage losses as a function of current density, showing accurate ANN prediction of activation ($\triangle\eta_a$, $\triangle\eta_c$) and ohmic ($\triangle\phi_e$, $\triangle\phi_p$) overpotentials.

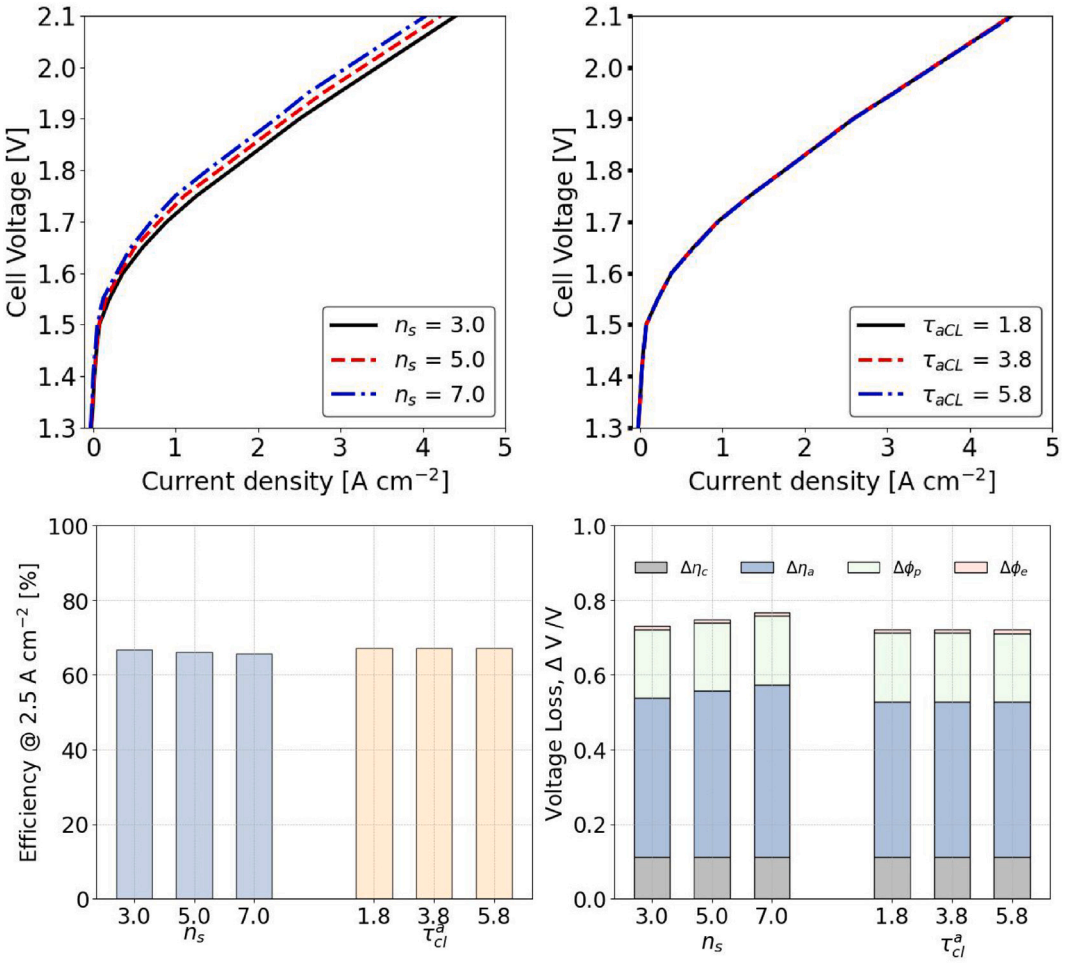


Fig. 5. Effect of structural properties on the cell performance and voltage losses. Top row: Polarization curves illustrating the influence of coverage exponent (n_s) (left) and catalyst layer tortuosity (τ_{aCL}) (right) for three representative values of each parameter. Bottom row: (left) corresponding cell efficiencies at 2.5 A cm^{-2} for different τ_{aCL} and n_s, and (right) decomposition of voltage losses under the same conditions, highlighting the relative contributions to voltage losses for each case.

the reaction sites. For the tested range of design parameters, we notice that τ^a_{cl} has no influence on cell performance.

The plots shown in the bottom row of Fig. 5 depict the cell efficiency and voltage losses at varying n_s and τ^a_{cl}. The values of η_{cell} and voltage losses were computed at a current density of 2.5 A/cm^2. A slight decrease in η_{cell} from 66.7% to 65.6% was noted when η_s is increased from 3.0 to 7.0. This is indicated by our observations of the polarization curve above, wherein a higher cell voltage is required to maintain the same current density. Similarly, η_{cell} remains constant across all τ^a_{cl} values. From the distribution of voltage losses for varying n_s, it is evident that the η_a is the primary driver of overall voltage losses. An increase of 8.2% in η_a is noted when we increase n_s from 3.0 to 7.0. This confirms the impact of n_s in penalizing anode electrode kinetics leading to higher overpotential. With the other voltage losses remaining constant across varying n_s, this shows that the ANN-II model is capable of relating coverage exponent as a parameter that exclusively influences the anode electrode kinetics, thereby retaining the physical consistency inherent in the training dataset.

Absolute permeability is the property of a material which governs the resistance to the flow of fluids through it, generally under a pressure gradient. It is a material property which depends on the microstructure characterized by the pore size and connectivity. Fig. 6 (top row) illustrates the influence of anode PTL and CL absolute permeability on the j-V relationship. At low current densities (< 1 A/cm^2), we observe that all curves overlap and show no dependence on absolute permeability. Since at such low current densities, the gas generation is small, the influence of capillary pressure gradient and gas pressure is weak. As κ^a_{ptl} is increased from 3.5×10^{-13} to 9.0×10^{-12} m^2, we observe a decrease in cell potential at higher current densities. We also note from the inset figure that the i-j relationship is very similar for higher values of κ^a_{ptl}, as shown for $\kappa^a_{ptl} = 2.5 \times 10^{-12}$ m^2 and 9.0×10^{-12} m^2. This indicates that beyond a certain permeability, the improvement in cell performance saturates. Similar to the effect of κ^a_{ptl}, we notice that the polarization curves overlap with each other with an increase in κ^a_{cl} at low current densities. At higher current densities, cell voltage decreases with an increase in κ^a_{cl}.

A slight gain in η_{cell}, from 66% to 67.5%, is observed when κ^a_{ptl} is varied from 3.5×10^{-13} to 2.5×10^{-12} at current density of 2.5 A/cm^2. However, a 3.8% increase in η_{cell} is noted when κ^a_{cl} is varied from 4.0×10^{-15} to 9.0×10^{-14}. To understand this difference in behaviour, a closer look at the distribution of various voltage losses for varying κ^a_{ptl} and κ^a_{cl} is needed. As κ^a_{ptl} increases, it facilitates ease with which oxygen gas bubbles are removed from the PTL. It also helps in easier counterflow of liquid water from the PTL to the anode CL, thereby, keeping the membrane hydrated and reducing proton ohmic resistance ($\triangle \phi_p$). As such, a reduction in 200 mV of $\triangle\phi_p$ is noted when κ^a_{ptl} is varied from higher to lower values. When κ^a_{cl} is small, the catalyst hinders the passage of generated oxygen. This creates gas holdup leading to strong capillary pressure within the catalyst layer. Moreover, steep saturation gradients are created within the thin anode CL. This results in higher anode overpotential losses with $\eta_a = 0.48$ V for $\kappa^a_{cl} = 4.0 \times 10^{-15}$. Conversely, as

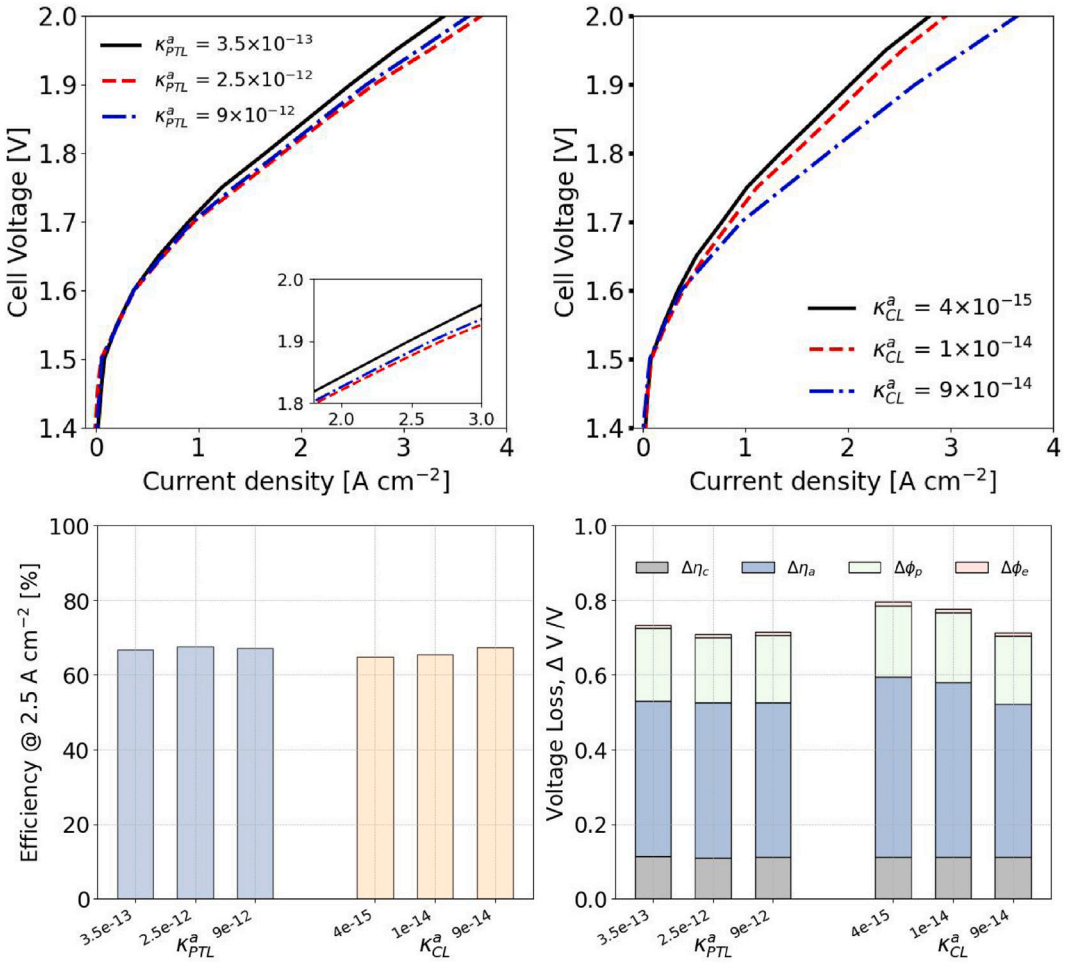


Fig. 6. Effect of structural properties on the cell performance and voltage losses. Top row: Polarization curves illustrating the influence of absolute permeability of anode side porous transport layer (κ^a_{PTL}) (left) and catalyst layer (κ^a_{CL}) (right) for three representative values of each parameter. Bottom row: (left) corresponding cell efficiencies at 2.5 A cm^{-2} for different κ^a_{PTL} and κ^a_{CL}, and (right) decomposition of voltage losses under the same conditions, highlighting the relative contributions of voltage losses for each case.

κ^a_{cl} increases, it improves the through plane gas-liquid counterflow and keeps the ionomer hydrated. This leads to reduction in $\triangle\phi_p$ (around 800 mV) as κ^a_{cl} increases.

The ionomer is a solid polymer with fixed sulphonic acid groups that facilitate proton mobility. Its primary role is to transport protons at the three-phase boundary where catalyst particles, ionomer and liquid water meet to perform the electrochemical reaction. When hydrated, the ionomer swells and influences the tortuosity of the catalyst layer. It fills in the pores and channels of the catalyst layer to reduce the effective gas liquid permeability and diffusivity. Fig. 7 illustrates the effect of ϵ^{ion}_{acl} on the polarization curve. With the initial part of the polarization curve governed by the electrode kinetics, the ionomer content does not influence the current density and all the three cases exhibit identical behaviour. The significance of ϵ^{ion}_{acl} on the i-j relationship becomes apparent at higher current densities. We observe a downward shift in cell voltage when ϵ^{ion}_{acl} is increased from 0.15 to 0.35. Further increase in ϵ^{ion}_{acl} to 0.55 shows slight decrease in cell voltage. At this point for high current densities (2–4 A/cm^2), the cell voltage is dominated by anode kinetics and two-phase transport, and not by membrane ionic resistance. A corresponding increase in η_{cell} from 65.5% to 67.3% is noted when ϵ_{mem} is varied from 0.15 to 0.35. Low ϵ_{mem} can prevent percolation of the ionomer phase into the catalyst layer, which leads to an increase in $\triangle\phi_p$. As we increase ϵ_{mem} from 0.15 to 0.55, the ionomer phase penetrates deeper into the porous network of the catalyst material. This results in the creation of better proton conducting pathways which lead to drop in $\triangle\phi_p$ from 0.24 V to 0.16 V.

3.4.2. *Effects of transport and electrochemical properties*

We now focus on the effect of the two transport and electrochemical properties, screened in SHAP analysis, on cell performance and voltage losses. The electronic conductivity controls how easily the electrons can move through the anode catalyst layer, and therefore, controls the loss of extra voltage to overcome this resistance. The top row of Fig. 8 illustrates the effect of σ^a_{cl} on the polarization curves for three different values. As observed for most of the parameters discussed above, all the three curves coincide for lower current densities (< 1.0 A/cm^2). This implies that the cell performance at this stage is predominantly governed by activation losses. The effect of σ^a_{cl} on cell voltage begins to be apparent as current density increases further, as depicted in the inset figure. The case with σ^a_{cl} = 6 S/m shows the poorest performance, while the other better performing cases overlap for the entire range of current densities. This indicates a saturation point wherein a further increase in σ^a_{cl} does not affect cell performance, as it is not limited by electronic resistance. The reference exchange current density ($j^{ref}_{o,a}$) is another kinetic property which depends on factors such as catalyst material, particle size, crystal arrangement and surface roughness. We notice that as $j^{ref}_{o,a}$ increases, the cell voltage decreases. It is interesting to note that $j^{ref}_{o,a}$ only affects the initial jump in cell voltage, after which we observe that

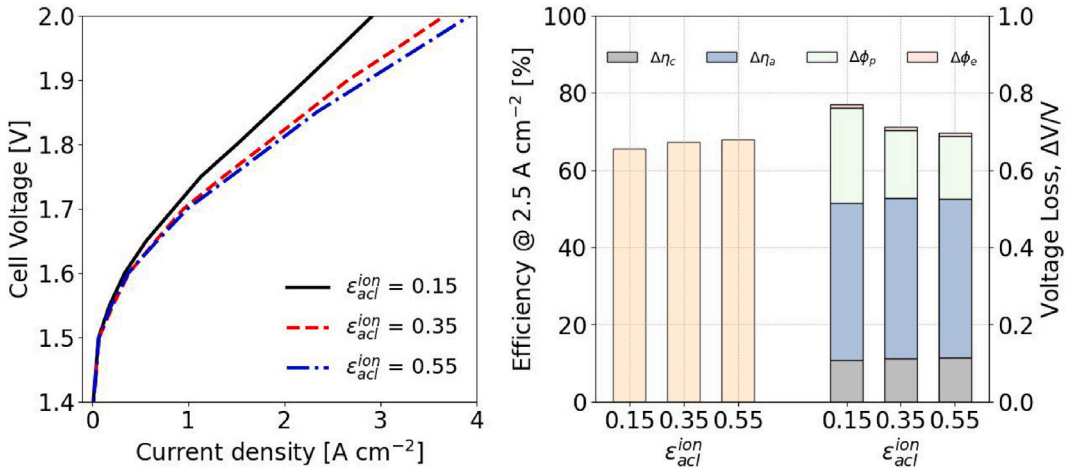


Fig. 7. Effect of structural properties on the cell performance and voltage losses. Right side: Polarization curves illustrating the influence of ionomer content in the anode catalyst layer (ϵ^{ion}_{acl}) for three representative values of this parameter. Left side: corresponding cell efficiencies at 2.5 A cm^{-2} and decomposition of voltage losses under the same conditions, highlighting the relative contributions of voltage losses for each case.

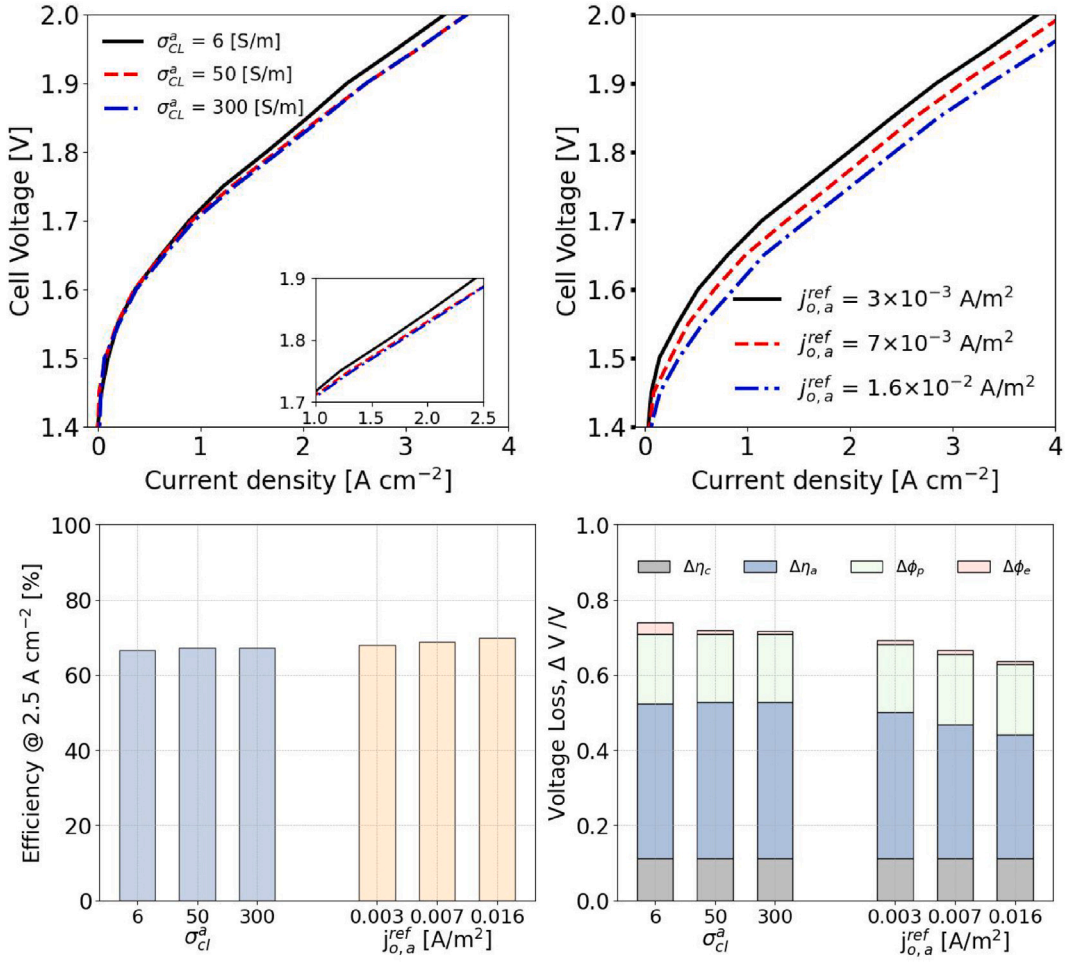


Fig. 8. Effect of physicochemical properties on the cell performance and voltage losses. Top row: Polarization curves illustrating the influence of electronic conductivity (σ^a_{cl}) (left) and reference exchange current density ($j^{ref}_{o,a}$) (right) for three representative values of each parameter. Bottom row: (left) corresponding cell efficiencies at 2.5 A cm^{-2} for different σ^a_{cl} and $j^{ref}_{o,a}$, and (right) decomposition of voltage losses under the same conditions, highlighting the relative contributions of voltage losses for each case.

all the three curves run parallel to each other. This is unlike that observed for σ^a_{cl}, where the curves for σ^a_{cl} = 6 S/m and σ^a_{cl} = 50 S/m begin to diverge at higher current densities. At a given current density of 2.5 A/cm^2, we notice that η_{cell} shows a marginal increment from 66% to 67% for varying σ^a_{cl}, as shown in Fig. 8 (bottom row). Similarly, an increment from 68% to 70% is noted when $j^{ref}_{o,a}$ is changed from 3×10^{-3} A/m^2 to 1.6×10^{-2} A/m^2. The effect of σ^a_{cl} on cell performance is elucidated by observing the voltage losses. A reduction in $\triangle\phi_e$ from 30 mV to 10 mV is noted when σ^a_{cl} is increased from 6 to 50 S/m. This implies that the ohmic resistance associated with electron transport decreases as electronic conductivity increases. The apparent saturation in cell performance at higher σ_{cl} is also reflected by the slight increase in $\Delta\phi_e$ from 8 mV to 10 mV as σ^a_{cl} increases by nearly an order of magnitude, from 50 to 300 S/m. Since $j^{ref}_{o,a}$ is a factor which controls activation overpotential, it influences the $\triangle\phi_e$. This is shown in bottom row of Fig. 8. We observe a 16% decrease in $\triangle\phi_e$ when $j^{ref}_{o,a}$ is increased from 3×10^{-3} A/m^2 to 1.6×10^{-2} A/m^2. At higher $j^{ref}_{o,a}$, reaction kinetics are faster and the barrier to start the reaction is low. Consequently, a lower cell voltage is required to achieve the same current density.

At higher current densities, the losses are dominated by ohmic resistance. Therefore, we observe almost parallel curves with a given offset distance from the corresponding polarization curves. The slope of these polarization curves reflects the ohmic resistance, which is constant for all the three considered cases.

Based on the above parametric analysis, we deduce that both ANN-I and ANN-II data driven models have made predictions which are grounded in underlying physical laws. The models have learned these patterns from the training dataset generated by a robust 1-dimensional physics based numerical model. The parametric analysis was performed on parameters that are different from those used in training, with certain parameter values lying outside the training domain. We have previously observed the capability of ANN to perform well at extrapolation from a different dataset generated from the same source [16]. Once trained, data-driven models are capable of delivering near-instant inference for hundreds of parameter combinations. Table 3 in the appendix shows the performance of the ANN-I model in performing interpolation and extrapolation based on the RMSE values. The predictions for current density obtained from the ANN-I model were compared with corresponding values obtained from the numerical model. The table shows the values of the parameters used for performing parametric analysis as discussed above. For all the extrapolation cases considered, an RMSE of less than 0.1 is observed.

3.5. Optimization: genetic algorithm

Parameter optimization is another iterative and evaluation intensive process during which the models have to be solved a large number of times. The use of data-based surrogate models executes this process efficiently by replacing repeated evaluations of robust physics-based numerical model, thereby significantly reducing the overall optimization cost while maintaining acceptable accuracy. To execute this, we have used *genetic algorithm* to integrate the ANN-I model as the objective function with the aim of maximizing current density. The seven parameters screened from the SHAP analysis in Section 3.1 and applied cell voltage were used as the parameters to be optimized. Genetic algorithm model parameters such as the population size, number of generations and mutation probability were set to 50, 40 and 0.2, respectively. The tournament size parameter was set to 3. The necessity of using a surrogate model for optimization is highlighted by the computational demand of genetic algorithm. With a population size and number of generations of 50 and 40, respectively, the algorithm performs 2000 evaluations of the objective function. The 1D model takes approximately 25 s to generate an 11-point polarization curve (1.5 V to 2.0 V in 0.05 V steps). With an assumption of equal convergence time per step, a single steady-state evaluation takes around 2.27 s. Therefore, the total time required to run these 2000 evaluations is around 75 min. In contrast, the surrogate based genetic algorithm takes 0.42 s to evaluate these 2000 runs. Both the calculations were performed on the same computer (12th Gen Intel Core i5-1245U, 10 Cores, 16 GB RAM). This represents a computational speed-up factor greater than 10,000, highlighting the necessity and efficiency of the surrogate framework for iterative parameter optimization.

Table 2
Baseline and optimized parameter values obtained through genetic algorithm based surrogate modeling optimization.

Property	n_s	κ^a_{ptl} [m^2]	κ^a_{cl} [m^2]	τ^a_{cl}	ϵ^{ion}_{acl}	σ^a_{cl} [S/m]	$j^{ref}_{o,a}$ [A/m^2]
Base	4	1×10^{-12}	5×10^{-14}	2.5	0.3	350.0	1×10^{-3}
Optimized	2	4.25×10^{-12}	7.5×10^{-14}	5.0	0.5	89.26	1.32×10^{-2}

Table 2 shows the values of the optimized parameters obtained through genetic algorithm. The optimized parameters show a decrease in n_s, and σ^a_{cl} values when compared to the corresponding values of the base parameters. An increase in κ^a_{ptl}, κ^a_{cl}, ϵ^{mem}_{cl} and $j^{ref}_{o,a}$ is noted. Fig. 9 (left) shows the comparison between polarization curves obtained with the base parameters and those through optimization. The polarization curves clearly illustrate the improved cell performance with optimized parameters. For example, at a current density of 2 A/cm^2 the cell voltage for the base and the optimized case are 1.82 V and 1.68, respectively. At lower current densities (< 0.5 A/cm^2), we observe that the cell voltage is lower with the optimized parameters. This indicates an improvement in activation losses. At higher current densities, we notice that the polarization curves gradually diverge, reflecting the decrease in losses due to ohmic resistance. The distribution of voltage losses shown in Fig. 2 (right) corroborates these observations. A decrease in $\triangle\eta_a$ from 41.5 mV to 33.4 mV is noted when the cell is operated with optimized parameters. Likewise, $\triangle\phi_e$ exhibits an improvement of 18.5% relative to the base case. These enhancements can be primarily attributed to the increased values of $j^{ref}_{o,a}$ and ϵ^{ion}_{acl} in the optimized configuration compared to the base case, which collectively contribute to improved electrochemical kinetics and reduced ohmic resistance.

To ensure that the genetic algorithm produced physically viable designs, upper and lower bounds were imposed on the seven design parameters, as provided in Table 1. The genetic algorithm subsequently maximized the ionomer volume fraction (ϵ^{ion}_{acl} = 0.5) and tortuosity (τ^a_{cl} = 5.0), thereby enhancing proton conductivity and increasing the current density. From a physical perspective, this result is consistent, as an increase in the ionomer volume fraction (ϵ^{ion}_{acl}) reduces the available pore space and creates a more restricted and tortuous transport network. Consequently, a high tortuosity value of 5.0 was obtained. However, evaluating the engineering applicability of these theoretically optimal values requires consideration of practical manufacturing constraints. Achieving an ionomer volume fraction of 50% is challenging with standard ink-based catalyst layer fabrication processes, as excessive ionomer loading can lead to ink agglomeration, electrical isolation of catalyst particles, and increased gas-transport resistance. Therefore, although the genetic algorithm identifies a pathway for maximizing current density through enhanced proton conductivity, a more conservative design with a lower ionomer volume fraction and corresponding tortuosity may be preferable to achieve a balance between theoretical performance and practical manufacturability.

4. Conclusions

This work investigates the role of anode-side structural and material properties on the performance of PEMWE using data-driven modeling. The models were developed using synthetic data generated from a 1D physics-based two-phase non-isothermal numerical model of PEMWE [23]. The dataset comprised a total of 13 input features with

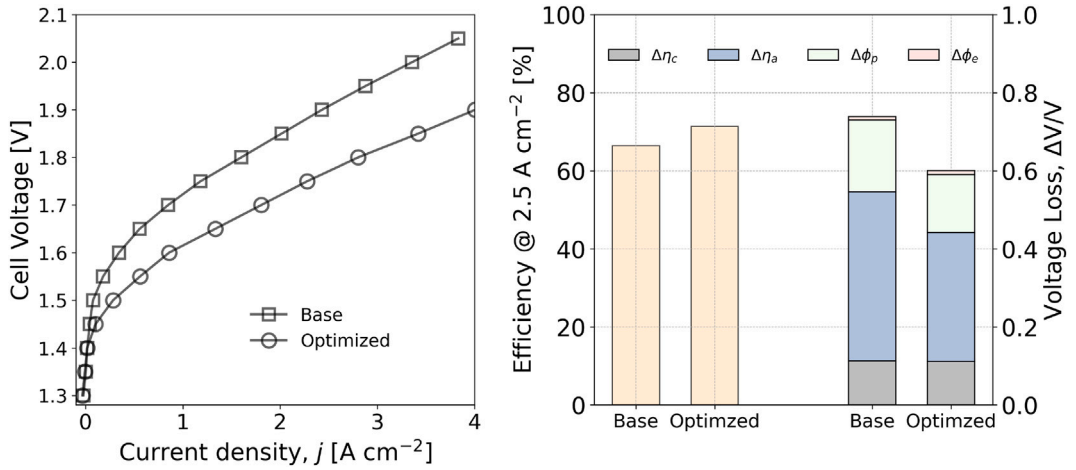


Fig. 9. Comparison between polarization curves (left), cell efficiency and voltage losses (right) obtained for base values (shown in Table 1) and those obtained through genetic algorithm based optimization using the surrogate model. The optimized parameters were obtained by using ANN-I as the objective function. The resulting optimized values of the structural and material properties were used to compute the voltage losses using ANN-II.

current density and voltage losses as output variables. The XGB model was first trained on the entire dataset and was used for SHAP analysis to screen influential parameters. Two ANN models were trained on the reduced dataset for predicting cell performance and voltage losses. The performance of all models was evaluated using RMSE and R^2 metrics. The main conclusions are as follows:

(1) SHAP-based feature selection is a useful technique to reduce dimensionality without compromising the predictive performance of the dataset. The initial dataset generated using full factorial design consisted of 21,140,071 data points. Application of SHAP-based feature selection reduced this to 65,026 data points representing a reduction of nearly 99% in dimensionality. This substantial compression improves computational efficiency in training ANN models, while retaining influential features.
(2) The usage of two ANN models to predict cell performance and voltage losses circumvents from the issue of *gradient imbalance*. While cell performance, represented by current density and thermoneutral efficiency, gives system information at a macroscopic cell level, voltage losses indicate the underlying mechanistic states. Therefore, decoupling them prevents the dominance of one target variable and ensures balanced updates of weights during backpropagation.
(3) Based on the selected set of input parameters, ionomer volume fraction and absolute permeability of the PTL were identified as the most important structural properties. Subsequent voltage loss decomposition showed variation in protonic and anodic overpotential losses as these parameters were systematically varied. In the case of material/phase intrinsic properties, the reference exchange current density was identified as the critical parameter.
(4) For the current set of input parameters, data-driven model aided parameter optimization directed toward increasing the ionomer volume fraction and the reference exchange current density to improve cell performance.

Tuning structural and material properties of catalyst and porous transport layers of PEMWE is essential not only to improve cell performance, but also to ensure commercial viability [49]. While extensive experimental data are required to accomplish such an investigation, data-based surrogate modeling using synthetic data is an efficient approach to accelerate initial design and screening process.

CRediT authorship contribution statement

K. Ashoke Raman: Writing – review & editing, Writing – original draft, Validation, Software, Methodology, Investigation, Formal analysis, Conceptualization. **Linus Hammacher:** Writing – review & editing, Software, Data curation. **Violeta Karyofylli:** Writing – review & editing, Investigation, Formal analysis. **Hans Kungl:** Writing – review & editing, Supervision, Project administration, Funding acquisition. **André Karl:** Writing – review & editing, Project administration. **Eva Jodat:** Writing – review & editing, Project administration. **Rüdiger-A. Eichel:** Writing – review & editing, Supervision, Project administration, Funding acquisition.

Declaration of competing interest

The authors declare that they have no known competing financial interests or personal relationships that could have appeared to influence the work reported in this paper.

Acknowledgements

The authors gratefully acknowledge the financial support from the German Federal Ministry of Research, Technology and Space (BMFTR) within the H_2Giga project DERIEL (grant number 03HY122 C). The authors gratefully acknowledge computing time on the supercomputer JURECA at the Forschungszentrum Jülich under the grant no. aipemec [50].

Appendix A. SHAP analysis of ANN-I model

To further validate the feature reduction, we performed SHAP analysis on ANN-I model to match the ranking of the seven selected features with those observed in Fig. 1(b) from the XGB model. Fig. 10 shows the SHAP rankings of the seven properties based on the ANN-I model. We observe that the ranking of the last three parameters (n_s, σ^a_{cl} and τ^a_{cl}) are same as those observed in Fig. 1(b). There is a shuffle in the ranking of the top four features, with $j^{ref}_{o,a}$ being considered the most important feature, followed by the ionomer content (ϵ^{ion}_{acl}). The permeabilities of catalyst and porous transport layers were the next two important features. The difference in the SHAP rankings of the top four features

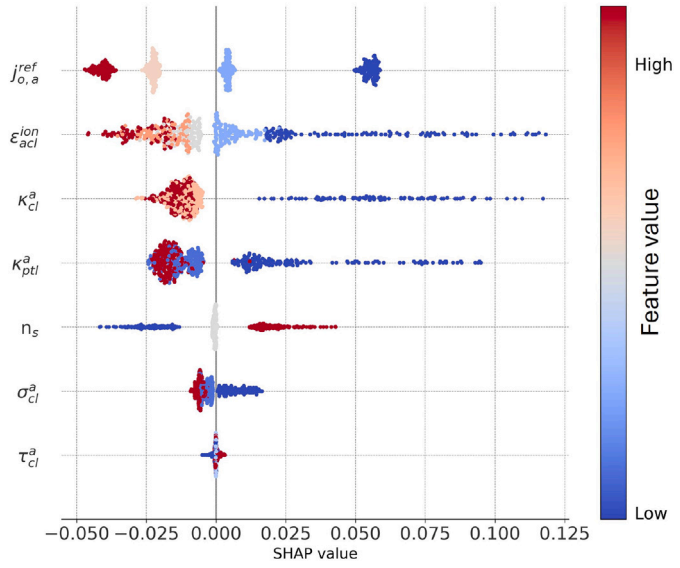


Fig. 10. Shapley additive explanations (SHAP) summary plots illustrating the relevant features and their influence in predicting cell voltage. The plots shown correspond to the ANN-I model developed from the reduced database.

can be attributed to the mathematical formulation of both the models. XGB performs feature isolation using orthogonal cuts in the feature space in order to minimize error at each split. ANN on the other hand maps feature importance through continuous gradients and non-linear activation weights. Additionally, XGB evaluates SHAP based feature importance by computing the contribution of each feature over the entire set of features whereas, feature importance using ANN is performed on a reduced dataset. The contribution of the minor features to the relative marginal weights of the ANN is reduced, resulting in the variations in the SHAP rankings. While the hierarchy of the dominant four parameters is shifted, both XGB and ANN models rank the remaining three features in the same exact order. This reinforces that, algorithmically, both models agree on the threshold for the features selected to reduce the dataset.

Appendix B

Table 3
The interpolation and extrapolation performance of ANN I model.

Parameter	Interpolation		Extrapolation	
	Value	RMSE	Value	RMSE
ϵ^{ion}_{acl}	0.15 0.35	0.0341 0.0246	0.55	0.0196
$j^{ref}_{o,a}$ [A/m^2]	3×10^{-3} 7×10^{-3}	0.0556 0.0502	1.6×10^{-2}	0.0450
ns	3 5	0.0243 0.0225	7	0.0274
τ^{a}_{cl}	1.8 3.8	0.0264 0.0296	5.8	0.0951
κ^{a}_{ptl} [m^2]	3.5×10^{-13} 2.5×10^{-12} 9.0×10^{-12}	0.0762 0.0622 0.0210	11.0×10^{-12}	0.0854
κ^{a}_{cl} [m^2]	4.0×10^{-15} 1.0×10^{-14}	0.1839 0.1846	9.0×10^{-14}	0.0217
σ^{a}_{cl} [S/m]	6 50 300	0.0392 0.0189 0.0174	400	0.0519

Data availability

Data will be made available on request.

References

[1] Javed A, Wolf NL, Meyer F, Treutlein L, Kungl H, Karl A, Jodat E, Eichel R-A. Exploring the state-of-operation of proton exchange membrane electrolyzers. Int J Hydrog Energy 2025;98:280–94.
[2] Yuan X-Z, Shaigan N, Song C, Aujla M, Neburchilov V, Kwan JTH, Wilkinson DP, Bazylak A, Fatih K. The porous transport layer in proton exchange membrane water electrolysis: perspectives on a complex component. Sustain Energy Fuels 2022;6(8):1824–53.
[3] Xu C, Wang J, Wang J, Yang K, Li G, Gao W, Wang H, Zhao S. Structural optimization study on porous transport layers of sintered titanium for polymer electrolyte membrane electrolyzers. Appl Energy 2024;357:122541.
[4] Hasa B, Aryal UR, Higashi S, Tolouei NE, Lang JT, Erb B, Smeltz A, Zenyuk IV, Zhu G. Porous transport layer influence on overpotentials in PEM water electrolysis at low anode catalyst loadings. Appl Catal B Environ Energy 2025;361:124616.
[5] Liu J, Kerner F, Schlueter N, Schroeder D. Predicting the topological and transport properties in porous transport layers for water electrolyzers. ACS Appl Mater Interfaces 2023;15(46):54129–42.
[6] Zinser A, Papakonstantinou G, Sundmacher K. Analysis of mass transport processes in the anodic porous transport layer in PEM water electrolysers. Int J Hydrog Energy 2019;44(52):28077–87.
[7] Lickert T, Kiermaier ML, Bromberger K, Ghinaiya J, Metz S, Fallisch A, Smolinka T. On the influence of the anodic porous transport layer on PEM electrolysis performance at high current densities. Int J Hydrog Energy 2020;45(11):6047–58.
[8] Wang Y, Wang H, Dong X, Du Y, He W, Zhao Y, Li H. Catalyst layer structure properties on hydrogen fuel generation performance of proton exchange membrane water electrolyzers. Fuel 2024;364:131040.
[9] Zhang H, Zhu J, Xu J, Wang C, Yuan H, Dai H, Wei X. Investigation on the influence of structural parameters in the porous transport layer on the mass transfer process within PEM water electrolyzer. Int J Heat Mass Transf 2025;253:127519.
[10] Hegge F, Moroni R, Trinke P, Bensmann B, Hanke-Rauschenbach R, Thiele S, Vierrath S. Three-dimensional microstructure analysis of a polymer electrolyte membrane water electrolyzer anode. J Power Sources 2018;393:62–6.
[11] Xu G, Du X, Que L, Zhang L, Li J, Ye D, Song J, Gao J. Optimization of anode porous transport layer in proton exchange membrane water electrolysis. Appl Therm Eng 2025;263:125384.
[12] Mandal M, Moore M, Secanell M. Measurement of the protonic and electronic conductivities of PEM water electrolyzer electrodes. ACS Appl Mater Interfaces 2020;12(44):49549–62.
[13] Bernt M, Schramm C, Schröter J, Gebauer C, Byrknes J, Eickes C, Gasteiger H. Effect of the IrOx conductivity on the anode electrode/porous transport layer interfacial resistance in PEM water electrolyzers. J Electrochem Soc 2021;168(8):084513.
[14] Heume C, Karyofylli V, Javed A, Dzieciol K, Basak S, Poc J-P, Tasdemir Y, Rutsch Y, Rein L, Wolf N, et al. Cross-plane iridium-based filaments SAP efficiency in proton exchange membrane electrolyzers. Joule 2026;10(2).
[15] Zhang Y, Xiang S, Yang Y, Van Haeverbeke M, Zhang J. Influence of electronic conductivity of the anode catalyst layer on proton exchange membrane water electrolysis. J Power Sources 2025;655:237911.
[16] Raman KA, Hammacher L, Kungl H, Karl A, Jodat E, Eichel R-A, Karyofylli V. Data-driven surrogate modeling for performance prediction and sensitivity analysis of transport properties in proton exchange membrane water electrolyzers. Appl Energy 2025;386:125529.
[17] Bock R, Karoliussen H, Seland F, Pollet BG, Thomassen MS, Holdcroft S, Burheim OS. Measuring the thermal conductivity of membrane and porous transport layer in proton and anion exchange membrane water electrolyzers for temperature distribution modeling. Int J Hydrog Energy 2020;45(2):1236–54.
[18] Burheim OS, Su H, Hauge HH, Pasupathi S, Pollet BG. Study of thermal conductivity of PEM fuel cell catalyst layers. Int J Hydrog Energy 2014;39(17):9397–408.
[19] Justin Jose Sheela AS, Wai Woo M, Marshall A, Kennedy J, Liu J. Critical factors contributing to thermally induced hotspots in PEM water electrolysers. J Electrochem Soc 2025;172(10):104510.
[20] Wang CR, Stansberry JM, Mukundan R, Chang H-MJ, Kulkarni D, Park AM, Plymill AB, Firas NM, Liu CP, Lang JT, et al. Proton exchange membrane (PEM) water electrolysis: cell-level considerations for gigawatt-scale deployment. Chem Rev 2025;125(3):1257–302.
[21] Karyofylli V, Danner Y, Raman KA, Kungl H, Karl A, Jodat E, Eichel R-A. Sensitivity analysis and uncertainty quantification in predictive modeling of proton-exchange membrane electrolytic cells. J Power Sources 2024;600:234209.
[22] Trinke P, Bensmann B, Hanke-Rauschenbach R. Experimental evidence of increasing oxygen crossover with increasing current density during PEM water electrolysis. Electrochem Commun 2017;82:98–102.
[23] García-Salaberri PA. 1D two-phase, non-isothermal modeling of a proton exchange membrane water electrolyzer: an optimization perspective. J Power Sources 2022;521:230915.
[24] Garcia-Navarro JC, Schulze M, Friedrich KA. Measuring and modeling mass transport losses in proton exchange membrane water electrolyzers using electrochemical impedance spectroscopy. J Power Sources 2019;431:189–204.
[25] Bhaskaran S, Pandey D, Surasani VK, Tsotsas E, Vidakovic-Koch T, Vorhauer-Huget N. LBM studies at pore scale for graded anodic porous transport layer (PTL) of PEM water electrolyzer. Int J Hydrog Energy 2022;47(74):31551–65.

[26] Lin R, Huo J, Cai X, Lan S, Hao Z. Numerical study of the effects of wettability and hierarchical porosity on oxygen transport within the porous transport layer of proton exchange membrane electrolyzers. J Power Sources 2024;614:235030.
[27] Ding R, Chen Y, Rui Z, Hua K, Wu Y, Li X, Duan X, Wang X, Li J, Liu J. Guiding the optimization of membrane electrode assembly in a proton exchange membrane water electrolyzer by machine learning modeling and black-box interpretation. ACS Sustain Chem Eng 2022;10(14):4561–78.
[28] Ding R, Zhang S, Chen Y, Rui Z, Hua K, Wu Y, Li X, Duan X, Wang X, Li J, et al. Application of machine learning in optimizing proton exchange membrane fuel cells: a review. Energy AI 2022;9:100170.
[29] Chen L, Tian Y, Hu X, Yao S, Lu Z, Chen S, Zhang X, Zhou Z. A universal machine learning framework for electrocatalyst innovation: a case study of discovering alloys for hydrogen evolution reaction. Adv Funct Mater 2022;32(47):2208418.
[30] Timmermann J, Kraushofer F, Resch N, Li P, Wang Y, Mao Z, Riva M, Lee Y, Staacke C, Schmid M, et al. IrO 2 surface complexions identified through machine learning and surface investigations. Phys Rev Lett 2020;125(20):206101.
[31] Flores RA, Paolucci C, Winther KT, Jain A, Torres JAG, Aykol M, Montoya J, Nørskov JK, Bajdich M, Bligaard T. Active learning accelerated discovery of stable iridium oxide polymorphs for the oxygen evolution reaction. Chem Mater 2020;32(13):5854–63.
[32] Chen X, Rex A, Woelke J, Eckert C, Bensmann B, Hanke-Rauschenbach R, Geyer P. Machine learning in proton exchange membrane water electrolysis—a knowledge-integrated framework. Appl Energy 2024;371:123550.
[33] Günay ME, Tapan NA, Akkoç G. Analysis and modeling of high-performance polymer electrolyte membrane electrolyzers by machine learning. Int J Hydrog Energy 2022;47(4):2134–51.
[34] Zimmer S, Wiesner F, Vollmert N, Steiger J, Engelhard T, Wessling M, Keller R. Data mining for enhanced PEM electrolysis. J Electrochem Soc 2026;173(2):024503.
[35] Yang R, Mohamed A, Kim K. Optimal design and flow-field pattern selection of proton exchange membrane electrolyzers using artificial intelligence. Energy 2023;264:126135.
[36] Mohamed A, Ibrahem H, Yang R, Kim K. Optimization of proton exchange membrane electrolyzer cell design using machine learning. Energies 2022;15(18):6657.
[37] Ozdemir SN, Pektezel O. Performance prediction of experimental PEM electrolyzer using machine learning algorithms. Fuel 2024;378:132853.
[38] Raman KA, Wolf NL, Javed A, Karyofylli V, Kungl H, Karl A, Jodat E, Eichel R-A. Evaluating activation strategies and their stability on PEM water electrolyzers using machine learning. Energy AI 2025;100623.
[39] Baseer MA, Singh H, Kumar P, Nascimento EGS. AI-driven surrogate modelling for simulating hydrogen production via proton exchange membrane water electrolysers. Int J Hydrog Energy 2025;127:462–83.
[40] Karyofylli V, Raman KA, Hammacher L, Danner Y, Kungl H, Karl A, Jodat E, Eichel R-A. Elucidating parasitic currents in proton-exchange-membrane electrolytic cells via physics-based and data-driven modeling. Electrochem Sci Adv 2025;e70000.
[41] Ozdemir SN, Pektezel O. A CFD-driven machine learning approach for predicting PEM electrolyzer performance. Fuel 2026;405:136479.
[42] Debe M, Hendricks S, Vernstrom G, Meyers M, Brostrom M, Stephens M, Chan Q, Willey J, Hamden M, Mittelsteadt C, et al. Initial performance and durability of ultra-low loaded NSTF electrodes for PEM electrolyzers. J Electrochem Soc 2012;159(6):K165.
[43] Chandesris M, Médeau V, Guillet N, Chelghoum S, Thoby D, Fouda-Onana F. Membrane degradation in PEM water electrolyzer: numerical modeling and experimental evidence of the influence of temperature and current density. Int J Hydrog Energy 2015;40(3):1353–66.
[44] Wang Y, Wang C-Y. A nonisothermal, two-phase model for polymer electrolyte fuel cells. J Electrochem Soc 2006;153(6):1193–200.
[45] Vetter R, Schumacher JO. Free open reference implementation of a two-phase PEM fuel cell model. Comput Phys Commun 2019;234:223–34.
[46] Brundiers S, Trinke P, Bensmann B, Hanke-Rauschenbach R. Model-based investigation of recombination interlayers in PEM water electrolysis: concentration profiles, efficiency, and operational limits. J Electrochem Soc 2024;171(7):074509.
[47] Guan X, Bai J, Zhang J, Yang N. Multiphase flow in PEM water electrolyzers: a mini-review. Curr Opin Chem Eng 2024;43:100988.
[48] Mohamed A, Ibrahem H, Kim K. Machine learning-based simulation for proton exchange membrane electrolyzer cell. Energy Rep 2022;8:13425–37.
[49] Karl A, Jodat E, Kungl H, Dobrenizki L, Schmid G, Geskes P, Eichel R-A. Water electrolysis facing the gigawatt challenge—comprehensive de-risking of proton exchange membrane and anion exchange membrane electrolyser technology; 2025.
[50] Thörnig P. JURECA: data centric and booster modules implementing the modular supercomputing architecture at Jülich supercomputing centre. J Large-Scale Res Facil JLSRF 2021;7:A182.